

An Ultra-Broadband Chirality Selective Metastructure Absorber using High Impedance Surface

Wei Zhang, Zhen Qiao, and Hai-feng Zhang*

In this paper, an ultra-wideband chirality selective metastructure absorber is proposed that enables differential absorption and reflection of circularly polarized waves in the terahertz (THz) range. The structure achieves circular dichroism (CD) by using asymmetrically split metal rings as fundamental meta-atoms. Most critically, the high impedance surface and air-resonant cavities are inserted separately in the meta-atoms and dielectric substrate to enhance CD and broaden the bandwidth of absorption. The metastructure absorber can achieve more than 90% absorption of right circularly polarized waves at 0.675–1.244 THz, and it can maintain more than 90% reflection of left circularly polarized waves at 0.607–1.229 THz without changing the direction of rotation. Besides, its CD can reach more than 80% at 0.687–1.213 THz with a relative bandwidth of 55.3%. Spin-selective absorption, which is closely related to breaking chiral symmetry, is investigated through power loss distribution, wide-angle incidence, and scan parameter optimization. The proposed strategy is further validated in the THz band, and the polarization selection and manipulation techniques can be applied to chiral sensing/radio-thermometry, circular polarization detectors/lasers, and molecular spectroscopy.

1. Introduction

Electromagnetic metamaterials, as an emerging artificial electromagnetic material or composite structure, are composed of periodically arranged combinations of subwavelength unitary structures. By structurally ordering electromagnetic metamaterials, control of incident electromagnetic waves can be achieved. Thus, realizing unusual physical properties not possessed by substances in nature, such as negative refractive index,^[1,2] electromagnetic stealth,^[3–5] the inverse Doppler effect,^[6–8] etc. Meta-material absorber, an important branch in the rapidly developing field of electromagnetic metamaterials research, has a bright future in electromagnetic compatibility,^[9] stealth technology,^[10] elimination of electromagnetic interference,^[11] and other aspects. In recent years, metasurfaces have shown promising


applications with their novel mechanisms and flexible structural designs.^[12] In addition, the rapid development of microfabrication technologies is capable of achieving to provide sub-micron precision well below the terahertz (THz) wavelengths. Its further advancement of the concept of THz metasurfaces provides promising and cost-effective devices for many emerging fields, such as THz plasmonic biosensors.^[13] Nowadays, metamaterials have developed from metasurfaces into metastructures, which come from a 2D structure to a 3D one. Since Landy et al. proposed a three-layer structured metastructure wiper in 2008,^[14] the demand for metastructure wipers has been growing. A variety of wipers have been designed, and the operating bands of wipers have been extended from microwave to THz,^[15] IR,^[16] and visible bands.^[17]

Most metastructure absorbers (MAs) are based on linearly polarized waves,

which allow multifrequency, broadband, tunable absorption from microwave to optical regions.^[18–20] MAs of circularly polarized waves (CPW) have not been extensively studied. Circular dichroism (CD), the differential absorption of left circularly polarized waves (LCPW) and right circularly polarized waves (RCPW) exists in nature like deoxyribonucleic acid and protein molecules^[21] and has a wide range of applications in practical fields. The reconstruction and study of chiral structures based on metastructures provide an adjustable approach for the realization of spin-dependent absorption molecules.^[22]

The most classical structure that can achieve CD is the helix structure.^[23] Besides, in 2016, Tang et al. designed a Y-type resonant cavity plasma MA with very distinct chiral polarization-selective absorption properties for differently polarized light at different resonance wavelengths.^[24] With the in-depth study of metastructure, more and more structures can achieve differential absorption of CPW, but few structures can absorb one type of CPW while modulating another type of CPW. Shang et al. designed a capacitor loaded in a circular open ring to achieve complete absorption of RCPW and complete reflection of LCPW.^[25] The chirality selective metastructure absorber (CSMA) is used to select the direction of reflection. However, those CSMA are realized either by drilling holes in the dielectric plate or by loading electronic components, which not only increases the processing difficulty but also is not easy to apply in higher frequency bands

W. Zhang, Z. Qiao, H.-feng Zhang
College of Electronic and Optical Engineering & College of Flexible Electronics
Nanjing University of Posts and Telecommunications (NJUPT)
Nanjing 210023, P. R. China
E-mail: hanlor@njupt.edu.cn

 The ORCID identification number(s) for the author(s) of this article can be found under <https://doi.org/10.1002/andp.202300029>

DOI: 10.1002/andp.202300029

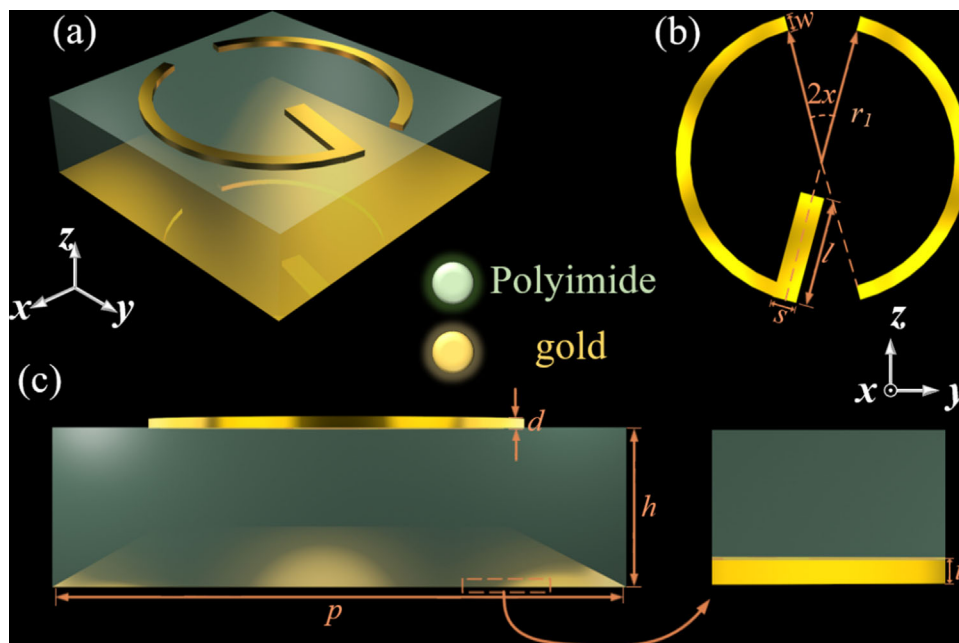


Figure 1. Schematic diagram of the meta-atom. a) The perspective view of the unit cell module, b) Top view of the upper metal resonator, and c) side view of the meta-atom. The optimized cell structure parameters are as follows: $p = 144 \mu\text{m}$, $x = 15^\circ$, $w = 6 \mu\text{m}$, $r_1 = 55 \mu\text{m}$, $s = 10 \mu\text{m}$, $l = 45 \mu\text{m}$, $d = 3 \mu\text{m}$, $h = 40 \mu\text{m}$, $t = 0.1 \mu\text{m}$.

(THz,^[26,27] IR,^[28] and optical visible spectral ranges^[29]). During the same period, Wang et al. constructed a CSMA by using an I-type resonator with asymmetric twisted metal wires.^[30] The absorption of LCPW can reach 95.18% and 91.77% at the two resonant frequencies, with little loss of RCPW. However, those meta-atoms can only do single-band or multi-band modulation, for ultra-broadband research is relatively rare.

Considering the current state of research today, we associate that the performance can be improved by loading high-resistance surfaces (HIS). Compared with conventional absorbing materials, the periodic absorbing structure designed based on an HIS has the advantages of ultra-thin thickness, wider bandwidth absorption, and the resistive film structure process is simpler to implement. Zhang et al. proposed an MA based on HIS with a periodic structure and demonstrated through theoretical and experimental studies that the thickness of the absorber was reduced by 41% and the absorption bandwidth of -15 dB was expanded by 50% compared to the conventional Salisbury absorber structure.^[31] The designed metal structure is replaced by a resistive film structure, which can convert electromagnetic resonance into circuit resonance. So far, many structures have been proposed. Gao et al. designed a novel radar-absorbing material using the Sevenpiper high impedance ground plane. The absorption performance of the radar-absorbing material is determined by the high impedance property.^[32] Wang et al. proposed an HIS-MA that has a wide absorption band of 12.14 GHz, from 6.86 to 19 GHz, with over 90% absorptivity at normal incidence.^[33]

Based on this, the HIS is used in the proposed CSMA, which can achieve ultra-broadband differential absorption for the CPW in the THz band while modulating the low-absorption CPW without changing the spin direction during reflection. In addition, the air-resonant cavities inserted in the metastructure expand the

bandwidth and the slit opened on the top metal resonator and the inserted metal plates can modulate the reflected CPW. Ultimately, it can achieve more than 90% of broadband absorption for RCPW at 0.675–1.240 THz, and main polarization reflection over 90% for LCPW can be obtained at 0.677–1.196 THz with a relative bandwidth of 55.4%.

2. Meta-Atom Design and Simulations

2.1. Theoretical Analysis and Simulation of the Initial Design

As indicated in **Figure 1a**, the proposed CSMA adopts the classical three-layer structure, consisting of an upper metal resonator, a bottom metal reflector, and an intermediate dielectric layer. The parameters of the upper “G-C” shaped periodic resonators are shown in **Figure 1b**. The G-type metal resonator is named part one, and the C-type metal resonator part is named part two. According to the requirements of the chiral structure, the model is designed to break both the n -fold ($n > 2$) rotational and mirror symmetries.^[34] A side view of the meta-atom can be seen in **Figure 1c**. The dielectric layer is polyimide with a relative dielectric constant of 3.5 and a tangential loss angle of 0.0027.^[35] The upper resonators and the bottom metal are both gold with a conductivity of $4.56 \times 10^7 \text{ S m}^{-1}$.^[36] The classical three-layer structure achieves an apparent chiral response by forming conduction currents within the metal surface. In contrast to three-layer structures, effective medium metasurfaces form displacement currents inside the superatoms, which in turn generate in-plane magnetic dipole moments to achieve the chiral response. Capasso’s group at Harvard University has used higher-order dipoles in dielectric nanostructures to achieve large circular dichroism in the visible light band.^[37] Near-infrared chiral medium metasurfaces have

also been proposed by several subject groups.^[38,39] However, in the terahertz band, the aforementioned scheme of processing high-refractive-index superatomic arrays on low-refractive-index substrates is difficult because of the thick thickness of the upper microstructure layer required. Although similar structures can also be achieved using bonding or adhesion, the processing is still difficult and the thickness is not easily controlled. So, choose to use gold as a conductive material, not only because it has the smallest loss in terahertz and higher frequency region, but also because it can better control the thickness and is easy to process.

Normally, fishnets and split-ring resonators highlight the realization of bulk electromagnetically induced transparency (EIT) analogs because of their effective medium characteristics.^[40] These artificial structures possess EIT-like resonances due to Fano-type linear destructive interference. However, the main study here is the absorption performance of such devices. In addition, the metal reflection layer at the bottom makes the transmission zero. The above structure is also broken after subsequent insertion into the HIS, thus losing the EIT signature.

According to the Jones formula, the incident and reflected electric fields have the following equations^[41]

$$\begin{pmatrix} E_r^+ \\ E_r^- \end{pmatrix} = \begin{pmatrix} r_{++} & r_{+-} \\ r_{-+} & r_{--} \end{pmatrix} \begin{pmatrix} E_i^+ \\ E_i^- \end{pmatrix} = R_{\text{circ}} \begin{pmatrix} E_i^+ \\ E_i^- \end{pmatrix} \quad (1)$$

where E_r refers to the reflected electric field and E_i refers to the incident electric field. Meanwhile, the “+” and “-” decibels indicate the clockwise and counterclockwise rotational waves when we observe in the +z direction, and in this case, they indicate the RCPW and LCPW, respectively. R_{circ} is the reflection matrix of a CPW, which can be represented by the reflection coefficients of a linearly polarized wave^[41]

$$R_{\text{circ}} = \begin{pmatrix} r_{++} & r_{+-} \\ r_{-+} & r_{--} \end{pmatrix} = \frac{1}{2} \times \begin{pmatrix} r_{xx} + r_{yy} + i(r_{xy} - r_{yx}) & r_{xx} - r_{yy} - i(r_{xy} + r_{yx}) \\ r_{xx} - r_{yy} + i(r_{xy} + r_{yx}) & r_{xx} + r_{yy} - i(r_{xy} - r_{yx}) \end{pmatrix} \quad (2)$$

where x and y represent the x -polarized waves and the y -polarized waves.

In addition, r_{++} and r_{--} represent the cross-polarization coefficients of RCPW and LCPW, respectively, and r_{-+} and r_{+-} represent the co-polarization reflection coefficients of RCPW and LCPW, respectively. There is no transmission in the reflective system because of the total reflection of the metal substrate. Then only the reflection can be considered in the calculation of the absorption coefficients^[42]

$$A_+ = 1 - (r_{++})^2 - (r_{-+})^2 \quad (3)$$

$$A_- = 1 - (r_{--})^2 - (r_{+-})^2 \quad (4)$$

For the differential absorption of CPW, we can characterize the CD^[42]

$$CD = A_+ - A_- \quad (5)$$

From the previous equations, when the incident RCPW is completely absorbed away and the LCPW is reflected by the main polarization, we can obtain the unique solution

$$\begin{pmatrix} r_{++} & r_{+-} \\ r_{-+} & r_{--} \end{pmatrix} = \frac{e^{i\alpha}}{2} \begin{pmatrix} 1 & i \\ i & 1 \end{pmatrix} \quad (6)$$

here, α is the phase.

Figure 2 shows the results of the simulation. From Figure 2a, it can be seen that the two absorption peaks of RCPW at 0.522 and 1.024 THz can reach 73% and 84% absorption, while the absorption rate of LCPW at the same frequency is only 20%. In addition, the absorption rate of RCPW is larger than that of LCPW in the simulated frequency range (0.45–1.15 THz), which means that there is still weak CD in the operating bandwidth range, except for the two absorption peaks. The weak polarization selective absorption indicates the possible existence of different absorption modes, offering us the possibility to enhance the differential absorption and extend the bandwidth. In Figure 2b, it can be concluded that since the surface impedance is the same for the CPW of different spins, their cross-polarization rates are the same. Similarly, Figure 2b illustrates that both low main polarization reflection peaks of the RCPW at 0.513 and 1.024 THz are below 40% and the main polarization reflectivity of LCPW is over 70%. It corresponds to the two high absorption peaks of RCPW and the low absorption bandwidth of LCPW in Figure 2a.

For both LCPW and RCPW resonance modes, we observe strong induced currents rotationally flowing in the meta-atom, suggesting a strong distortion effect on the optical field when a CPW of appropriate chirality passes through the metastructure. The meta-atom can be considered a coupled resonator system, where the strong chiral response comes from the coupling between the two arcs, and this effect is better reflected in the current diagram when the system is in resonance. When the LCPW is incident, its strong current is excited in the right arm of the metal at 0.522 THz, and the current flowing in the same direction is excited in both arms of the metal at 1.02 THz, as depicted in Figure 2c,d. The difference is that when the RCPW is incident, the reverse current is excited in both arms at 0.522 THz, and the current flowing against each other is excited in both the upper left and lower right positions of the metal at 1.02 THz, as illustrated in Figure 2e,f. These features of the current distribution suggest that the meta-atom excites antisymmetric and symmetric modes at the resonances of the RCPW and LCPW, respectively. Since the antisymmetric mode represents a higher energy in the coupled system than its symmetric mode, this is in agreement with numerical and experimental observations.

2.2. Broadband Selective Absorption Achieved by HIS

As mentioned before, the absorption rate of RCPW is always greater than that of LCPW in the simulated frequency range, and the CD is always positive. It can be assumed that the currents induced by RCPW and LCPW are different, and this is also confirmed in Figure 2. As a result, the HIS is inserted in the surface metal resonators, expecting to enhance the surface ohmic loss after RCPW incidence in the operating frequency, while not

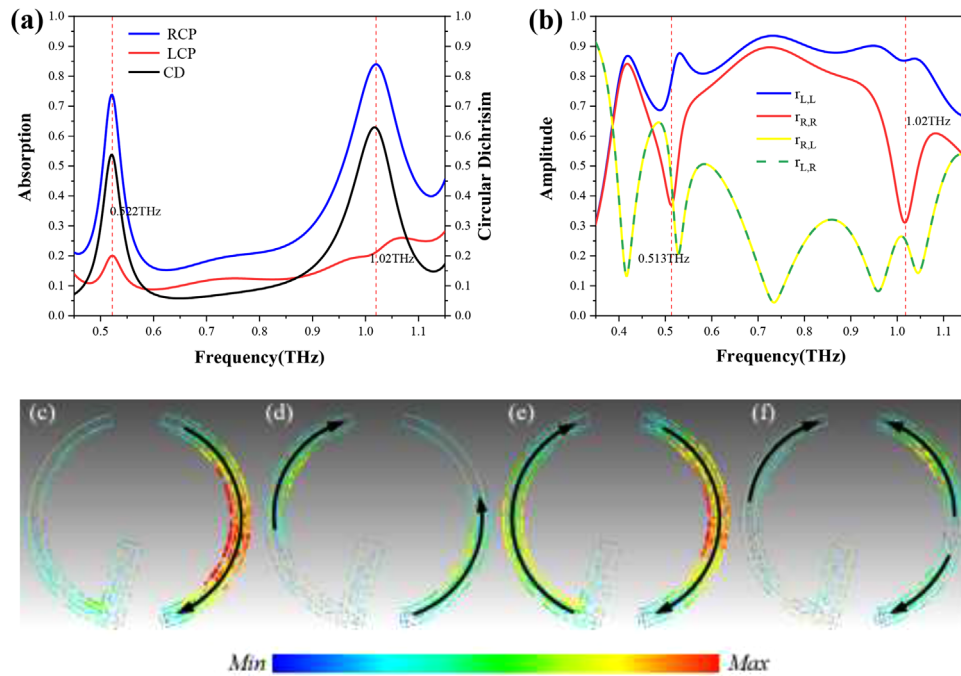


Figure 2. The simulated results of the meta-atom and magnitude distributions of the surface current. a) The simulated absorptivity, CD, and b) reflectivity of RCPW and LCPW. c) The distributions of the surface current for LCPW illumination on the top layer at 0.52 THz, d) at 1.02 THz, e) the distributions of the surface current for RCPW illumination on the top layer at 0.52 THz, and f) at 1.02 THz.

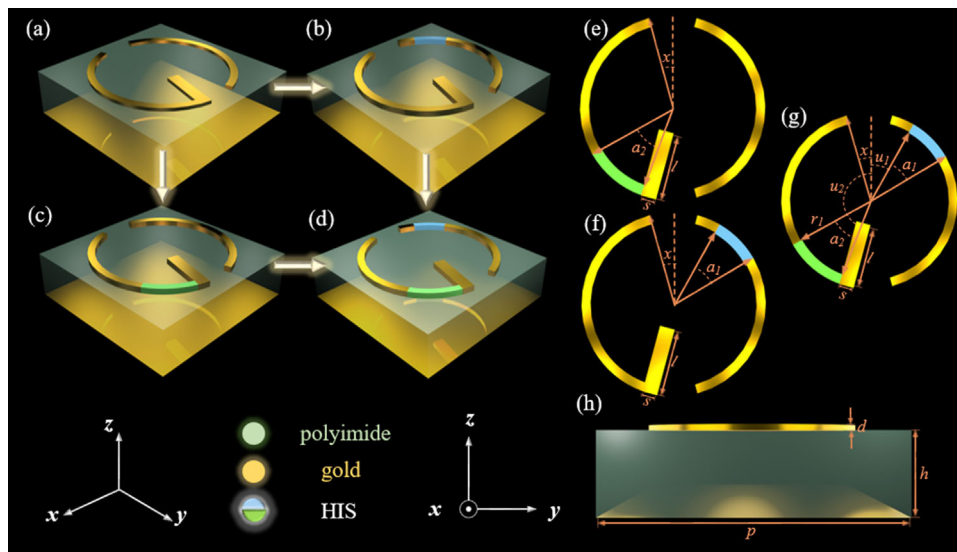


Figure 3. Schematic diagram of the optimization process of the designed structure. a) The schematic diagram of the meta-atom, b,c) meta-atoms that are inserted into one HIS each, (d) is the combination of (b) and (c). (e–g) correspond to the top view of the upper metal cavity of (c), (b), and (d), respectively. h) The side view of the structure. The optimized parameters are as follows: $x = 15^\circ$, $u_1 = 30^\circ$, $u_2 = 160^\circ$, $a_1 = 30^\circ$, $a_2 = 40^\circ$, $r_1 = 55 \mu\text{m}$, $l = 45 \mu\text{m}$, $s = 10 \mu\text{m}$, $p = 144 \mu\text{m}$, $h = 40 \mu\text{m}$, $d = 5 \mu\text{m}$.

affecting LCPW. At the same time, the asymmetric insertion of the HIS may enhance the chirality and improve the differential absorption capability. Considering the surface impedance, the high resistance will adjust the surface impedance of RCPW and LCPW incidents to achieve impedance matching and impedance mismatch. According to the surface current of the meta-atom,

two places are chosen to insert the HIS, shown in **Figure 3**, both are curved and articulated with metal resonators.

It is clear from **Figure 4a,b** that the absorption performance of RCPW increases to 80% at 0.52 THz with a wider absorption peak than the original one after inserting a high resistor in part one. Similarly, at 1.024 THz the absorption peak even forms a narrow

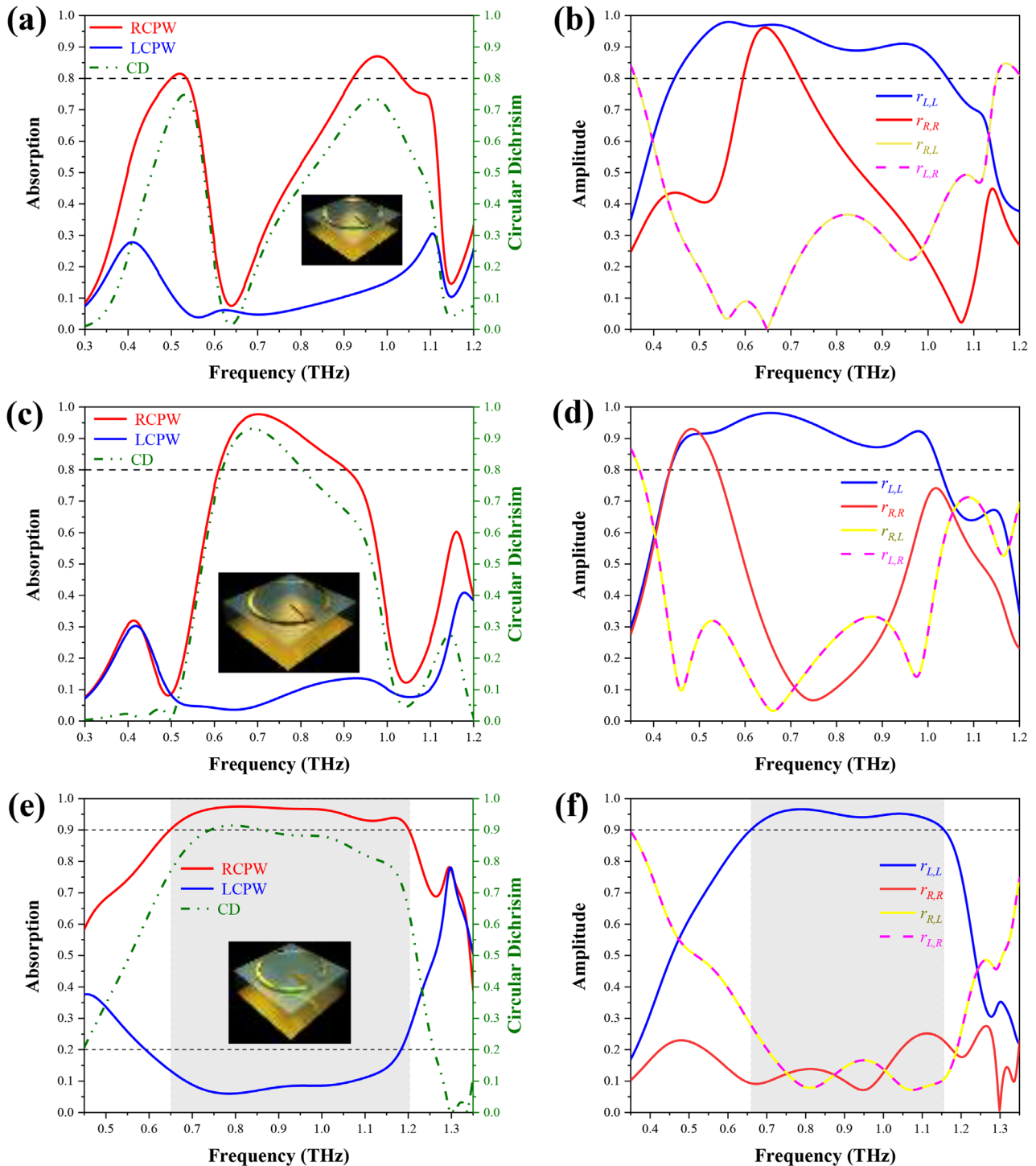


Figure 4. The simulated results of the meta-atom after insertion of the HIS. a) The curves of absorptivity, CD, b) the reflectivity of the structure after insertion of the HIS in part one, c) the curves of absorptivity, CD, d) the reflectivity of the structure after insertion of the HIS in part two, e) the curves of absorptivity, CD, and f) the reflectivity of the structure after insertion of the HIS in part one and two.

absorption band at 0.920–1.034 THz with the redshift to 80% at the top. In addition, the HIS forms a better impedance match, which reduces the cross-polarization coefficient of the CPW to less than 20% in the range of 0.496–0.708 THz and achieves a better reflection performance of the LCPW. In Figure 4c,d, the

RCPW achieves more than 80% broadband absorption at 0.615–0.916 THz and up to 98% absorption peak at 0.706 THz after inserting the HIS in part two. In addition, the HIS optimizes the surface impedance and reduces the cross-polarization of the CPW wave in the range of 0.550–0.826 THz, and the LCPW can

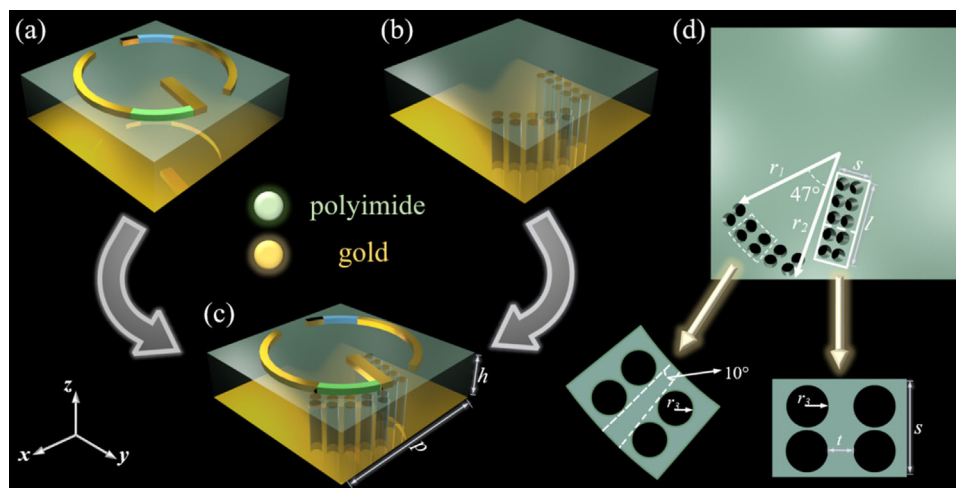


Figure 5. The schematic diagram of the optimization process of the designed structure. a) The schematic diagram of the meta-atom after insertion of the HIS, b) the dielectric substrate with air-resonant cavities inserted, c) the structure diagram of the meta-atom with air-resonant cavities inserted, and d) the top view of the dielectric substrate with air-resonant cavities inserted. The optimized structure parameters are as follows: $p = 144 \mu\text{m}$, $h = 40 \mu\text{m}$, $r_1 = 55 \mu\text{m}$, $r_2 = 71 \mu\text{m}$, $r_3 = 2 \mu\text{m}$, $t = 3 \mu\text{m}$, $s = 10 \mu\text{m}$, $l = 45 \mu\text{m}$.

reach 90% of the main polarization reflection in the range of 0.470–0.854 and 0.945–1.000 THz. It can be seen that the addition of the HIS enhances the chirality of the structure and forms a better differential absorption. The HIS provides the structure with stronger surface ohmic loss, which successfully enhances the absorption performance of RCPW and even improves the main polarization reflectivity of LCPW. The two seemingly opposite capabilities can be accomplished by chirality.

As presented in Figure 4e,f, the absorptivity and reflectivity curves of CPW are obtained by inserting the HIS of Figure 4a,c into the structure at the same time. The CSMA achieves an ultra-broadband absorption of RCPW from 0.646 to 1.202 THz over 90%, while the absorption of LCPW can be maintained below 20% from 0.56 to 1.184 THz. The absorption bands of RCPW formed by the HIS can be just staggered to form an ultra-broadband after superposition. And the coupling between them can enhance the amplitude of each other's absorption peaks, finally achieving the desired effect. The suitable high resistance value regulates the surface impedance and suppresses the spin of the structure so that the main polarization reflection of LCPW is more than 90% in the range of 0.658–1.156 THz.

2.3. To Improve Performance using Air-Resonant Cavities

The improved structure diagram is observed in Figure 5c. Figure 5a,b depicts the CSMA with the HIS and the dielectric substrate with air-resonant cavities inserted. Figure 5d illustrates the geometric parameters of the air-resonant cavities on the dielectric substrate. The air-resonant cavities are divided into two parts, the rounded section is used to strengthen the local absorption of RCPW around the HIS in part one, and the square part is used to strengthen the resonance around the metal strip.

After inserting the air-resonant cavities, it can be seen that the RCPW absorptivity curves plotted in Figure 6a flattens out and improves at the high-frequency end, and the LCPW absorptivity

also decreases significantly. In Figure 6b, it can also be observed that the bandwidth of the main polarization reflection coefficient for LCPW becomes wider and has a little blue shift. The improved absorption bandwidth of RCPW increases by nearly 0.03 THz at high frequencies and the LCPW also gains 0.045 THz in the main polarization reflection bandwidth.

In the method of broadening the bandwidth by adding the air-resonant cavities in the medium, it would be more appropriate to explain it in terms of a power density diagram. Figure 6c,d plots the top view of the electric energy density intensity at the surface of the structure, which shows the electric energy density decreases at the surface of the air-resonant cavities. Looking at the cross-sectional electric energy density diagram of the structure (Figure 6e,f), the air-resonant cavities have a limiting effect on the electric field. And the electric field energy is extended down the air column by a length, which increases the loss in the medium and thus enhances the absorption. In addition, since the resonant frequency is lower in the resonant cavity, and there is no resonant cavity below the metal sheet, a photon localization effect is produced and the refractive index is thus changed. This is more pronounced in the high-frequency range, so the blue shift can be seen at high frequencies, and the bandwidth increases.

2.4. The Optimization Process of CSMA by Opening Slits in the Metal Ring

To weaken LCPW absorption and enhance primary polarization reflection, opening slits has been done in the metal ring. The optimization process of the structure is manifested in Figure 7. The initial structure is in Figure 7a, the air-resonant cavities and embedded high resistance are added in Figure 7b, and then finally in Figure 7c, we try to open the slits on the metal resonator and insert metal plates. We open the slits near the connection of the HIS and the metal resonator, then insert the metal plate on both sides of the slits. Figure 7d,e illustrates the top view and geometric

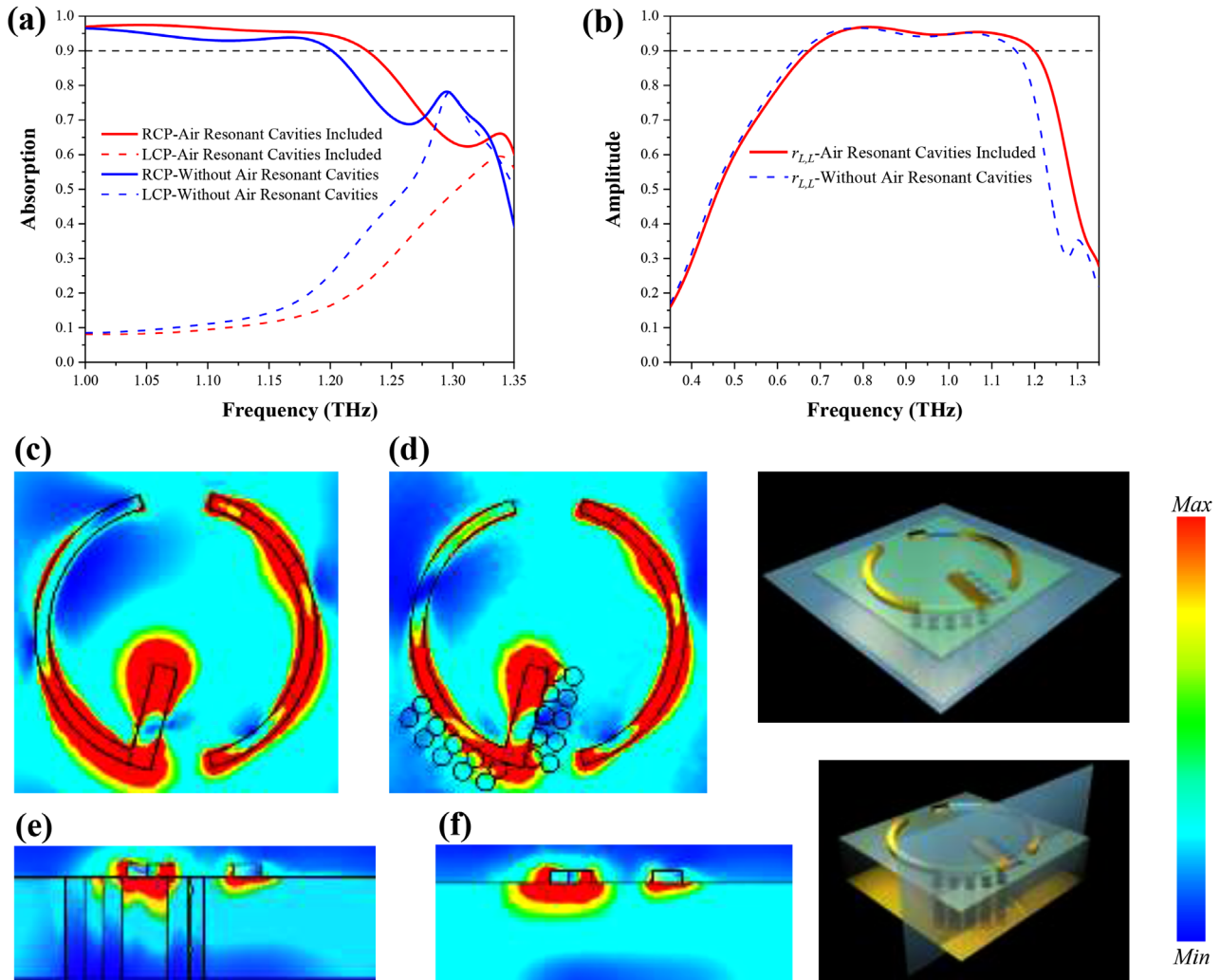


Figure 6. The simulated results and electric energy density diagrams for structures before and after adding the air-resonant cavities at 1.22 THz. a) The absorptivity, and b) the reflectivity of the structure before and after insertion of the air-resonant cavities. c,d) The simulated distributions of electric fields in the x - y plane, and e,f) the simulated distributions of electric fields in the x - z plane.

parameters of the upper plus metal cavities before and after the opening of the slits.

In **Figure 8a**, after adding the slits, we drop the LCPW absorption curve to below 20% at the low-frequency end, but at the same time, the RCPW absorptivity decreases around 0.9 THz. The drop in LCPW absorptivity at low frequencies provides an opportunity for a possible 2D planar structure superposition to achieve ultra-wideband later. At the same time, in **Figure 8b**, LCPW can achieve 85% of the main polarization reflection in the range of 0.528–1.214 THz. Similarly, 2D planar structure superposition would allow LCPW high-effectiveness reflections to be achieved over a wider bandwidth.

The absorption of LCPW is attenuated by adding slits and metal plates in the metal ring, which can be clearly explained by the surface current diagram. As observed in **Figure 8d**, the surface resonant current is regulated by inserting slits and metal plates between the high resistance and the metal ring. The slits can block the conduction of surface current, thus weakening the current strength on the HIS and reducing the ohmic loss. The

weakened resonant current can be seen in the part circled by the red dashed line in **Figure 8**, which is coincident with the position where we insert the HIS. However, the current reduction effect of the gap is too obvious, then may change the resonant mode of the surface and the frequency point, so we add the metal plates to adjust the effect of the slits.

3. Results and Discussion

Since the structure of Section 2.4 weakens the absorption of RCPW after the addition of slits and metal plates, the structure of Section 2.3 inserted by HIS and air-resonant cavities is chosen as the final version on balance. The final version, shown in **Figure 7b**, achieves a circularly polarized differential absorption bandwidth of 0.56 THz and a primary polarized reflection bandwidth of 0.525 THz for the LCPW. In the absorption state, the operating bandwidth can range from 0.665 to 1.218 THz, and the absorption performance of the RCPW is above 90%, while the absorption performance of the LCPW can be kept below 20%. In the

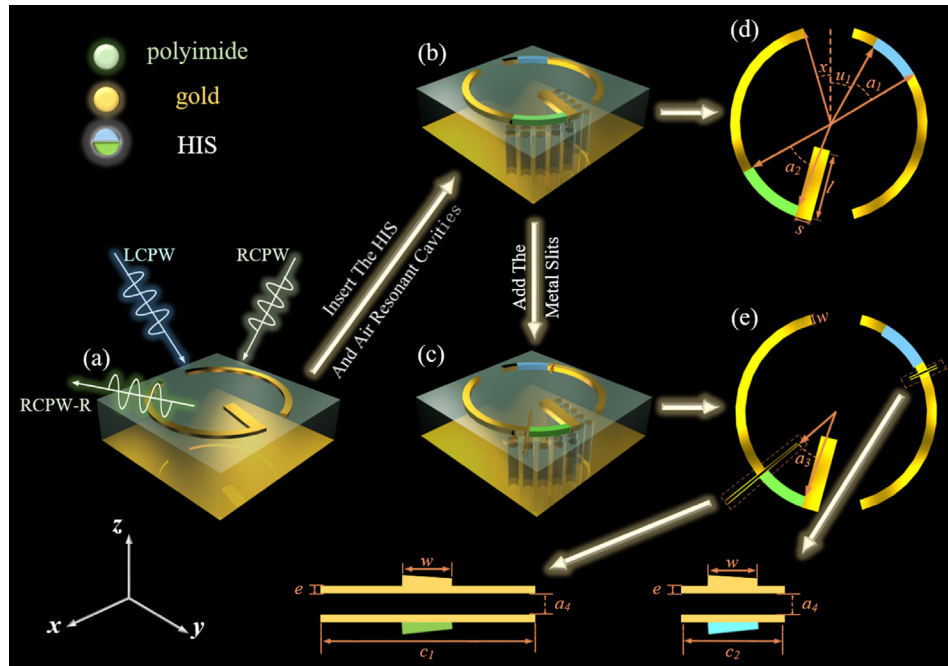


Figure 7. The optimization process for structural insertion of slits and metal plates. a) The initial structure, b) the schematic diagram after insertion of the HIS and the air-resonant cavities in (a), c) the schematic diagram of the structure with the slits in the metal ring based on (b), and (d) and (e) are the top views and geometric parameters of the upper metal cavities corresponding to (b) and (c), respectively. The optimized structure parameters are as follows: $x = 15^\circ$, $u_1 = 30^\circ$, $u_2 = 160^\circ$, $a_1 = 30^\circ$, $a_2 = 40^\circ$, $a_3 = 30^\circ$, $r_1 = 55 \mu\text{m}$, $l = 45 \mu\text{m}$, $s = 10 \mu\text{m}$, $w = 6 \mu\text{m}$, $e = 0.5 \mu\text{m}$, $a_4 = 1^\circ$, $c_1 = 25 \mu\text{m}$, $c_2 = 6 \mu\text{m}$.

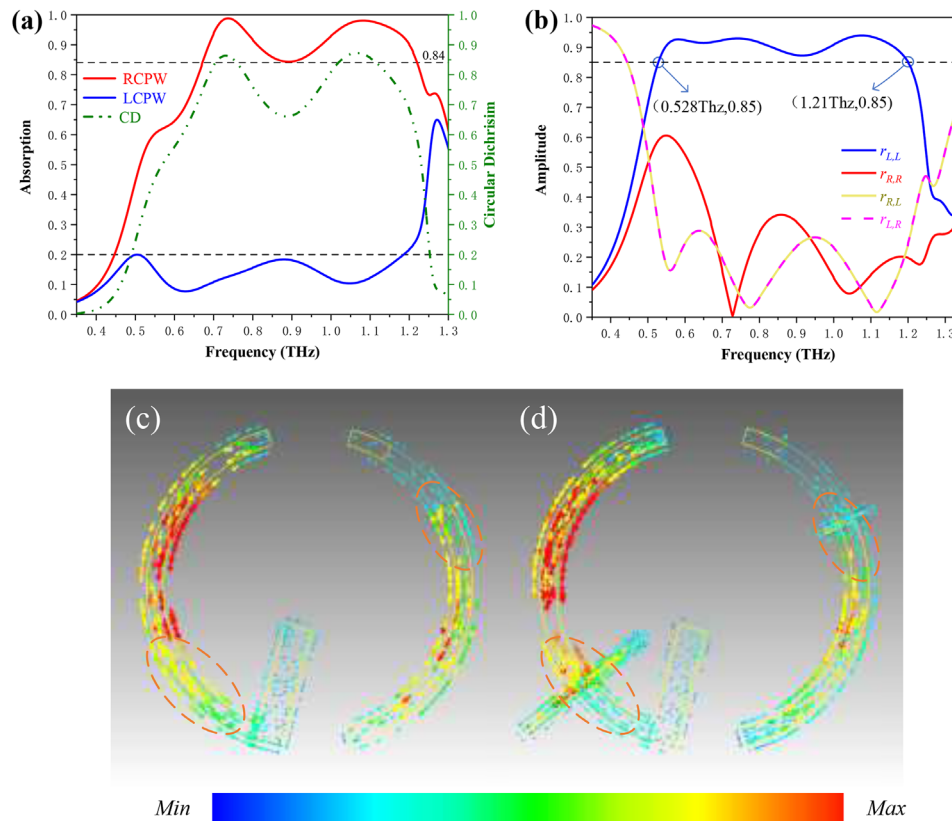


Figure 8. a) The curves of the simulated absorptivity, CD, and b) the curves of reflectivity of the structure after adding the metal slits. c) The simulated induced surface current distributions of the top metal resonant structures on the total resonant cell before adding slits and metal plates, and d) after adding slits and metal plates.

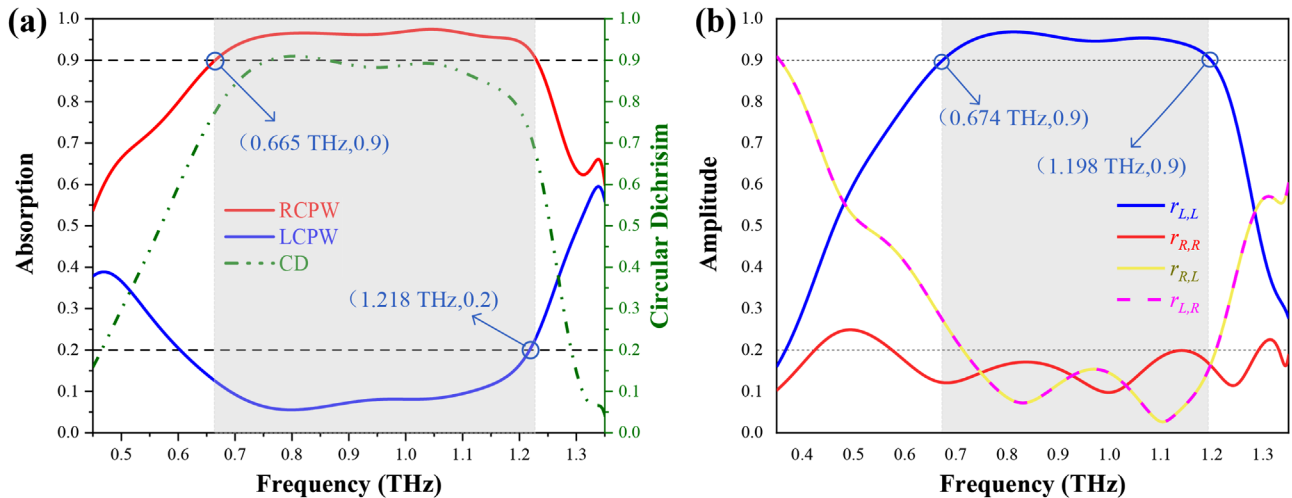


Figure 9. The absorption and reflection spectra of final optimized CSMA. a) The curves of simulated absorptivity, CD, and b) the curves of reflectivity of the final version.

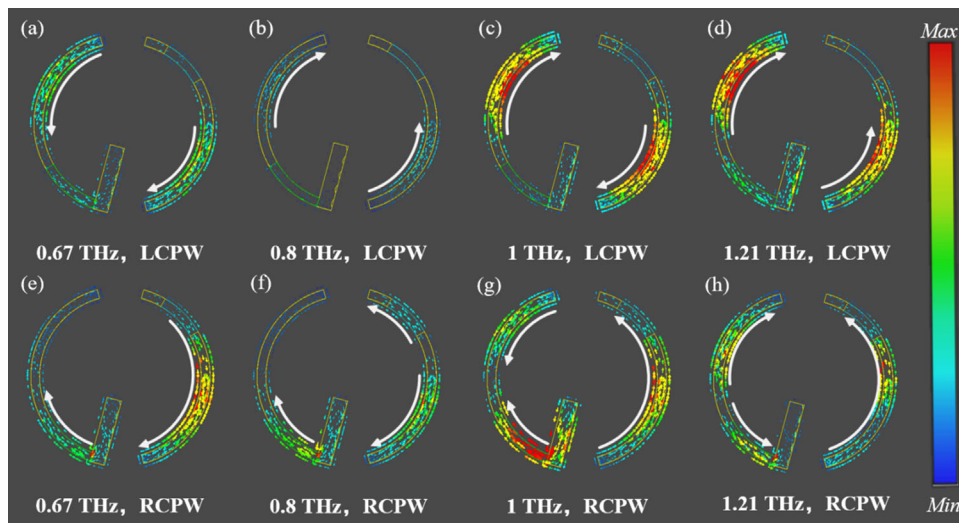


Figure 10. The induced surface current distributions of the top metal resonant structures on the total resonant cell. a–d) The surface current distributions of the top metal pair at LCPW incidence. e–h) The surface current distributions of the top metal pair at RCPW incidence.

reflection state, the operating bandwidth can range from 0.674 to 1.198 THz, and the main polarization reflectivity of LCPW can exceed 90%. These can be gotten from the following **Figure 9**.

3.1. Physical Mechanism

As shown in **Figure 10**, the upper metal has a significant difference in the excitation current for different spins of the CPW. From **Figure 10a,d**, it can be found that when the LCPW is incident, the resonant currents excited are distributed on the upper left and lower right sides of the metal ring, whether at low frequencies such as 0.67 THz or high frequencies at 1.21 THz, or intermediate frequency bands like 0.8 and 1 THz. This can explain why the insertion of high resistance has only a small effect on the LCPW, which still maintains a low absorption characteristic. In this mode, the high-intensity currents all avoid the HIS

inserted in the structure, and the symmetrical pattern formed by the currents in the same direction represents a lower energy loss. As depicted in **Figure 10e,h**, when the RCPW is incident on the surface of the structure, the resonant current is generated only on the lower left side of the metal ring, except at a frequency of 0.67 THz. At the same frequency as when the LCPW is incident, the RCPW produces an excitation current in the opposite direction on both the lower left and upper right sides. The reversed current excites the magnetic dipole oscillator, which generates magnetic resonance loss. Because the excitation current flows through the high resistance, it can generate huge ohmic loss and play a high absorption performance to the RCPW.

As elucidated in **Figure 11**, we can see that the “G-C” shaped metal resonator has optical absorption at different sites at different resonance wavelengths. The results indicate that different interactions between CPW and chiral metal resonators can induce

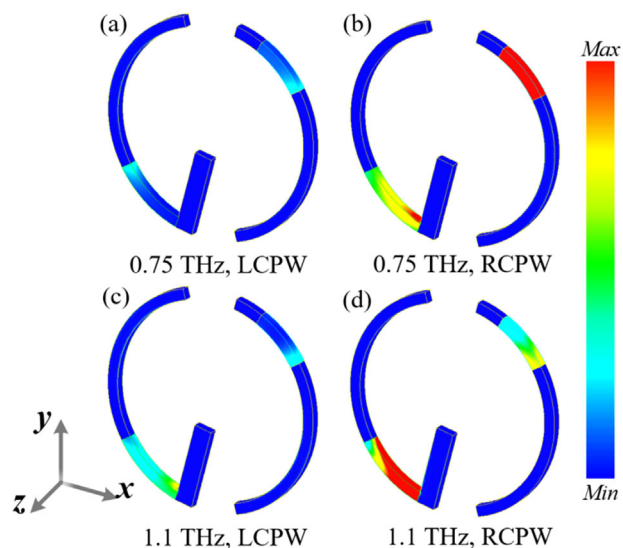


Figure 11. 3D absorbed power distributions for the CSMA. a) The power loss of the top metal pair at LCPW incidence at 0.75 THz and c) 1.1 THz. b) The power loss of the top metal pair at RCPW incidence at 0.75 THz and d) 1.1 THz.

different chiral currents inside the metal molecule, which directly leads to different chiral current resonance absorption. As shown in Figure 11a,c, LCPW has no strong resonance absorption at 0.75 and 1.1 THz. While RCPW has a stronger resonance absorption at the same frequency in Figure 11b,d.

3.2. Parameters Discussion

During the optimization of the structural parameters, several parameters are found to significantly affect the performance: the resistance values in part one ou_1 and the resistance values in part two ou_2 of the inserted HIS, and the thickness h of the polyimide. Other parameters have relatively small effects on the performance and are not discussed here. Since high resistance is the key to achieving broadband absorption, we will first focus on the impact of the change in the high resistance values. **Figure 12a** shows that the absorptivity of RCPW decreases in the frequency range around 0.7 THz when ou_1 is smaller than 100 ohm sq^{-1} , and the absorption bandwidth greater than 90% narrows from 0.800 to 1.223 THz. And when ou_1 becomes larger to 800 ohm sq^{-1} , the absorption drops to 80% in the frequency range between the two absorption frequency points, e.g., at 0.8 THz. Also at 1200 ohm sq^{-1} , the absorption rate of RCPW in the frequency range between the two absorption frequency points even drops to only 72%, and broadband absorption cannot be achieved. In **Figure 12b**, when ou_2 is 10 or 20 ohm sq^{-1} , there is a weakening effect on the absorption band around 1.1 THz, and the absorption rate drops substantially, reaching only 82%. And after ou_2 increases upward to 160 ohm sq^{-1} , it has a weakening effect on the whole operating band, reaching 90% absorption only in the range of 1.10 to 1.18 THz over the whole operating band. The addition of high resistance affects the strength of the resonant current, and a suitable resistance value maximizes the ohmic loss of the surface. Likewise, because of the complete asymmetry of

the structure, the two high resistances affect different operating frequencies and therefore have different resistance values. The different resistance values once again enhance the chirality of the structure and provide a better effect on CD. In addition, the appropriate high resistance value will adjust the surface impedance, and RCPW incidence can achieve the impedance matching requirements, in the LCPW incidence plays the role of impedance mismatch.

As observed in **Figure 12c,d**, with the increase of the dielectric layer thickness, the absorption performance of the structure in the high-frequency operating frequency domain of the THz band for RCPW and the reflection performance for LCPW is gradually enhanced. The best performance of the structure in the THz band is reached when $h = 40 \text{ }\mu\text{m}$. Its absorption rate in the frequency domain of 4.9–9.8 THz is higher than 90% with a relative bandwidth of 66.66%. As h continues to increase, the RCPW absorption rate and LCPW reflection rate of the structure in the whole operating frequency domain decrease to below 90%, and the frequency spectrum of the structure performance shifts toward high frequencies with the increase of h .

3.3. Large Angle Insensitivity

For the designed ultra-broadband CSMA, large angle insensitivity is likewise an important index that must be considered. The absorption spectra for an incident angle change from 0° to 90° are shown in **Figure 13**. In **Figure 13a**, when the incident angle is not greater than 45° , the absorption bandwidth of RCPW is only a little less than that of vertical incidence. But after greater than 45° , the absorption bandwidth changes into a double-peaked absorption bandwidth. Moreover, in **Figure 13b**, the reflectivity of LCPW is always able to reach 90% in the broadband range as the angle increases, which shows that the change of the incident angle has a small effect on the reflectivity of the main polarization of LCPW. Even at the narrowest width of the absorption band, a strong main polarization reflection from 0.706 to 1.095 THz is still achieved. In short, in the range of incidence angle less than 45° , although there is a tendency for the width of the absorbing frequency end of RCPW to decrease, by and large, it remains a broadband characteristic. When the incident wave is incident at a certain angle, the external chiral characteristics are also satisfied, and the CD pictogram may be enhanced at one time due to the phase difference arising from the different times of arrival of the wave train at the surface of the structure. It can be seen from **Figure 13** that the CSMA has a good wide incidence angle feature.

3.4. Effective Impedance

Nowadays, we have more methods to study effective impedance. In this work, the effective impedance of the CSMA is extracted based on S-parameters by the inversion method and further analyzed. Early on, Smith et al.^[43] proposed an electromagnetic calculation method in a paper, i.e., the inversion method of equivalent electromagnetic parameters. After continuous improvement by researchers, this method has been relatively mature, and its basic principle process is as follows.^[42]

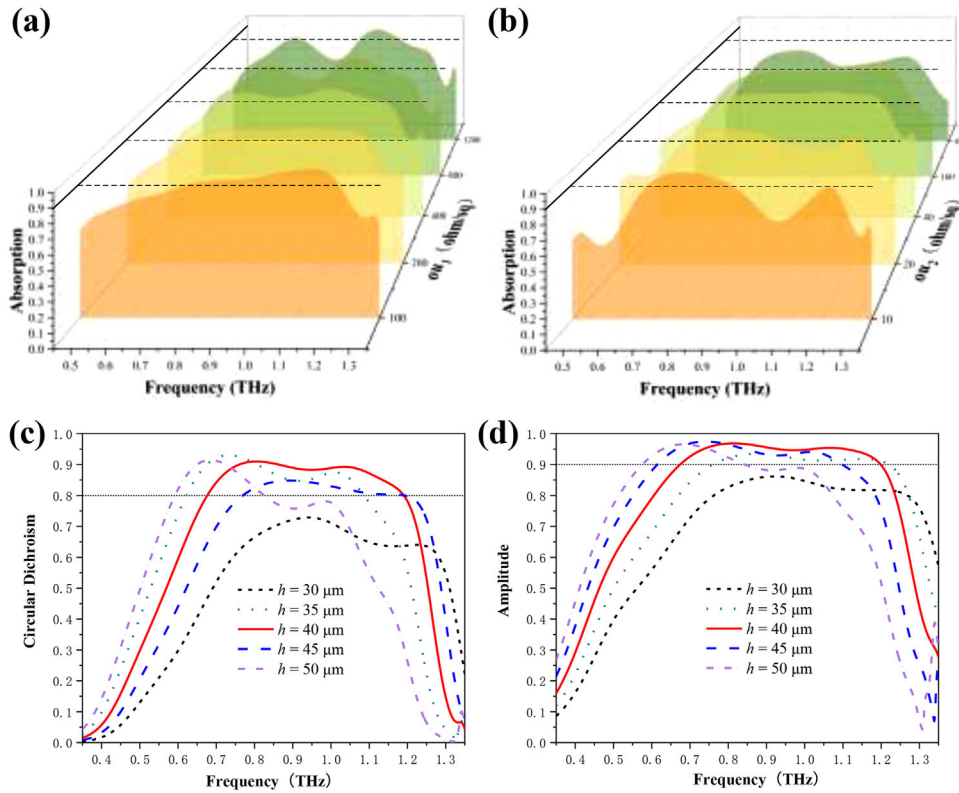


Figure 12. The dependence of the absorption curves on the high resistance values. a) The absorption curves corresponding to different high resistance values ou_1 , and b) ou_2 . c) The RCPW absorption spectra, and d) the LCPW reflection spectra for different media thicknesses.

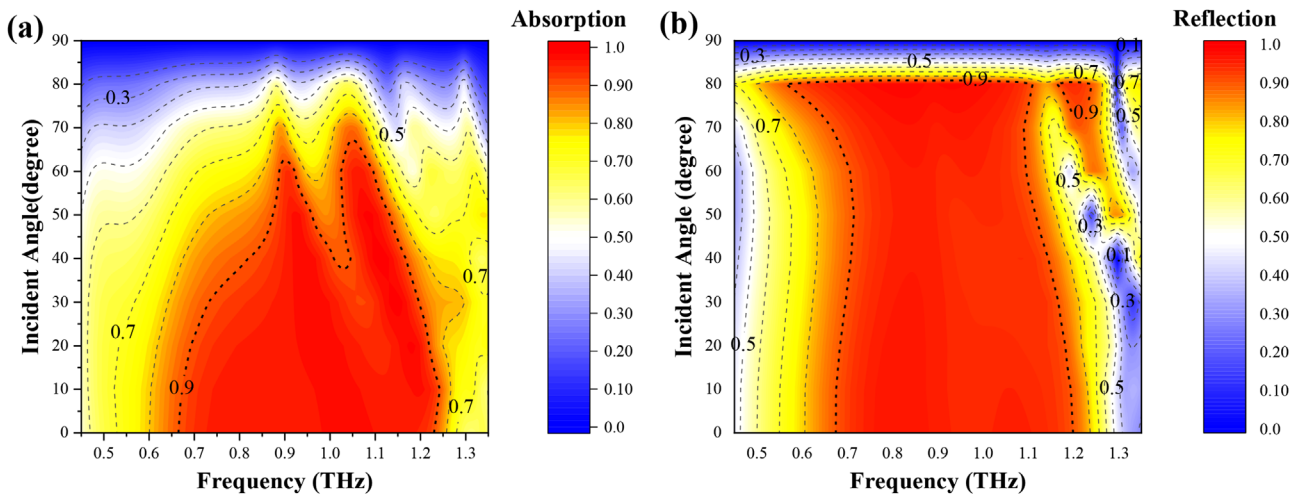


Figure 13. The dependence of the absorption and reflection curve on the incident angle varying from 0° to 90° . a) The RCPW absorptance, and b) the LCPW main polarization reflectance at different incidence angles.

For a homogenous metastructure, his transport matrix can be expressed as

$$T = \begin{pmatrix} \cos(nkd) & -\frac{z}{k} \sin(nkd) \\ \frac{k}{z} \sin(nkd) & \cos(nkd) \end{pmatrix} \quad (7)$$

where n is the refractive index and z is the wave impedance.

Since the transmission matrix T is difficult to measure directly, the magnitude of the scattering parameter S and the value of the phase parameter can be measured quickly by other methods. And the matrices T and S are related as follows

$$S_{21} = \frac{2}{T_{11} + T_{22} + \left(ikT_{12} + \frac{T_{21}}{ik} \right)} \quad (8)$$

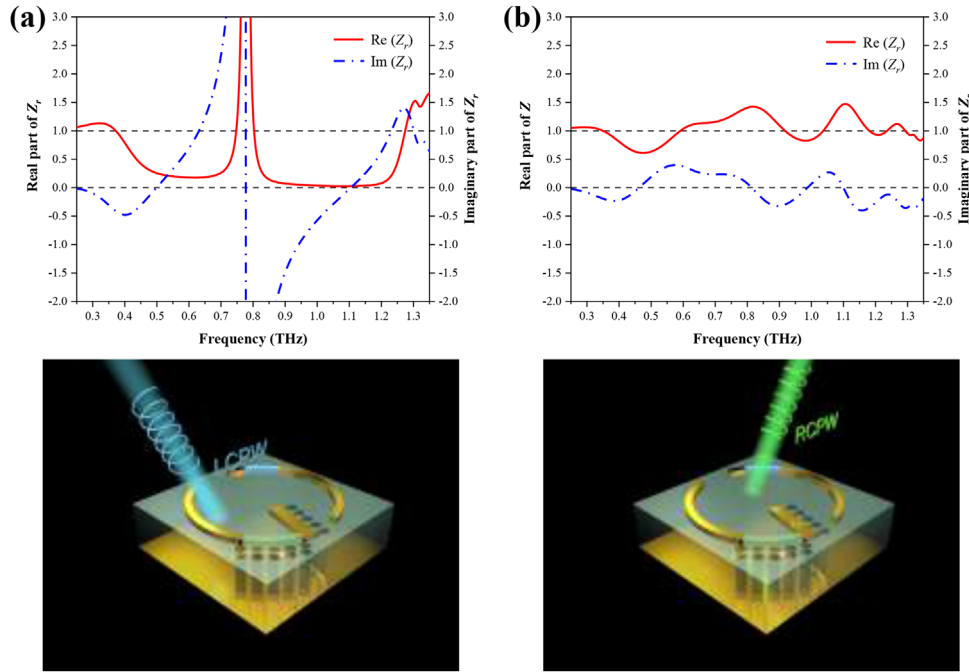


Figure 14. The effective impedance under a) LCPW incidence, and b) RCPW incidence.

$$S_{11} = \frac{T_{11} - T_{22} + \left(ikT_{12} - \frac{T_{21}}{ik} \right)}{T_{11} + T_{22} + \left(ikT_{12} + \frac{T_{21}}{ik} \right)} \quad (9)$$

$$S_{22} = \frac{T_{22} - T_{11} + \left(ikT_{12} - \frac{T_{21}}{ik} \right)}{T_{11} + T_{22} + \left(ikT_{12} + \frac{T_{21}}{ik} \right)} \quad (10)$$

$$S_{12} = \frac{2 \det(T)}{T_{11} + T_{22} + \left(ikT_{12} + \frac{T_{21}}{ik} \right)} \quad (11)$$

Also for a homogenous metastructure, it shows $T_{11} = T_{22} = T_s$ and $\det(T) = 1$

$$\det(T) = \begin{vmatrix} \cos(nkd) & -\frac{z}{k} \sin(nkd) \\ \frac{k}{z} \sin(nkd) & \cos(nkd) \end{vmatrix} = 1 \quad (12)$$

so S is a symmetric matrix. Thus

$$S_{21} = S_{12} = \frac{1}{T_s + \frac{1}{2} \left(ikT_{12} + \frac{T_{21}}{ik} \right)} \quad (13)$$

$$S_{11} = S_{22} = \frac{\frac{1}{2} \left(\frac{T_{21}}{ik} - ikT_{12} \right)}{T_s + \frac{1}{2} \left(ikT_{12} + \frac{T_{21}}{ik} \right)} \quad (14)$$

Bringing the parameters in the matrix T into the above equation gives the S parameters

$$S_{21} = S_{12} = \frac{1}{\cos(nkd) - \frac{i}{2} \left(z + \frac{1}{z} \right) \sin(nkd)} \quad (15)$$

$$S_{11} = S_{22} = \frac{i}{2} \left(\frac{1}{z} - z \right) \sin(nkd) \quad (16)$$

By inverting the two equations, the equivalent impedance is obtained

$$z = \sqrt{\frac{(1 + S_{11})^2 - S_{21}^2}{(1 - S_{11})^2 - S_{21}^2}} \quad (17)$$

As illustrated in **Figure 14a**, in the case of LCPW incidence, the real part of the equivalent impedance of CSMA is close to 0 in the range of 0.45–1.25 THz, and the imaginary part is also almost not equal to 1, satisfying the condition of impedance mismatch. In contrast, in **Figure 14b**, when RCPW is incident, the real part of the equivalent impedance floats above and below 1, and the imaginary part fluctuates around 0, which satisfies the impedance matching requirement well.

3.5. Simulation Methods and Settings

Numerical simulation results were obtained using the commercial simulation software High Frequency simulation software (HFSS). Master-slave boundary conditions are applied in both the x and y directions to simulate such an infinite period structure, and two Floquet ports are placed on the upper and lower surfaces

Table 1. Comparison of the proposed work with previous reports.

Ref.	Incident wave	Active material	Structural features	Functionality	Performances and frequencies
[21]	y-polarized waves and CPW	gold	bi-layered complementary Y-shaped	90° polarization rotation and giant CD effect simultaneously	2.12 THz: 90° linear polarization rotation of y-polarized waves 2.38 THz: transmission coefficient for RCPW of 0.82, transmission coefficient for LCPW of 0.15
[22]	CPW	silicon dioxide	N-shaped	chiral selective absorption	the CD magnitude approaches ≈ 0.5 at the wavelength of 643 and 760 nm
[23]	CPW	resistances	capacitive loading of metal circular split rings	chiral selective absorption	2.47 GHz: RCPW absorption of 97.2%, LCPW absorption of 24.6%
[28]	CPW	copper	I-shaped	chiral selective absorption and broadband plan conversion with dual bands	12.04 GHz: LCPW absorption of 95.18%, RCPW absorption of 17.2% 14.22 GHz: LCPW absorption of 91.77%, RCPW absorption of 22.3% 9.55–14.75 GHz: RCPW plan conversion
This work	CPW	HIS	"G-C"-shaped	ultra-broadband chiral selective absorption and total reflection	0.675–1.24 THz: RCPW absorption over 90% 0.607–1.229 THz: LCPW reflection over 90%

for the realization of electromagnetic wave radiation and reception. In this model, we set master-slave boundary conditions to simulate such an infinite period structure. The Floquet ports are set on the upper surface and incident vertically on the CPW. In addition, the fast sweep is used for the sweep, which gives a more accurate description of the field at the resonant frequency. When using the fast sweep, we select the center frequency of the frequency band as the adaptive grid dissection rate, perform the grid division, and calculate the *S*-parameter and field distribution at that frequency point. Then, the special solver is used to extrapolate the *S*-parameter and field solutions for the entire frequency band range from the *S*-parameter solution and field solution at the center frequency.

Finally, to systematically and visually describe the novelty and impact of this work, we summarize the relevant chiral selective devices with superior performance reported in recent years in **Table 1**. The structure in this paper has ultra-broadband strong CD and the ability to modulate the nonabsorbing CPW. In general, the CSMA proposed in this work is advanced and valuable compared with the listed research works.

4. Conclusion

In this paper, the CSMA is designed. The meta-atom uses an insertion method into the HIS to achieve broadband circularly polarized selective absorption and reflection. When a suitable resistance value is set for the high resistance, impedance matching for RCPW and impedance mismatching for LCPW can be achieved simultaneously. The absorptivity of RCPW can exceed 90% at 0.675–1.24 THz, while the absorptivity of LCPW is very low, resulting in significant absorptive CD. CSMA not only can strongly absorb RCPW illumination but also achieves spinless reflection of LCPW over a wide bandwidth (0.607–1.229 THz). Besides, the selected absorption and reflection mechanism, as well as the effects of incidence angle change and structural parameters change on the effects were analyzed by surface current maps, electric field intensity maps, and power loss maps of the device.

Conflict of Interest

The authors declare no conflict of interest.

Data Availability Statement

The data that support the findings of this study are available on request from the corresponding author. The data are not publicly available due to privacy or ethical restrictions.

Keywords

circular dichroism, circular polarization waves, high impedance surfaces, metastructure absorbers, ultra-broadband absorption

Received: January 18, 2023

Revised: February 19, 2023

Published online:

- [1] D. R. Smith, W. J. Padilla, D. C. Vier, S. C. Nemat-Nasser, S. Schultz, *Phys. Rev. Lett.* **2000**, *85*, 2933.
- [2] R. A. Shelby, D. R. Smith, S. Schultz, *Science* **2004**, *305*, 788.
- [3] D. Schurig, J. J. Mock, B. J. Justice, S. A. Cummer, J. B. Pendry, A. F. Starr, D. R. Smith, *Science* **2006**, *314*, 977.
- [4] U. Leonhardt, *Science* **2006**, *312*, 1777.
- [5] S. A. Cummer, B. I. Popa, D. Schurig, D. R. Smith, J. Pendry, *Phys. Rev. E* **2006**, *74*, 036621.
- [6] E. J. Reed, M. Soljačić, J. D. Joannopoulos, *Phys. Rev. Lett.* **2003**, *91*, 133901.
- [7] S. H. Lee, C. M. Park, Y. M. Seo, C. K. Kim, *Phys. Rev. B* **2010**, *81*, 241102.
- [8] K. M. Leong, A. Lai, T. Itoh, *Microwave Opt. Technol. Lett.* **2006**, *48*, 545.
- [9] S. Liu, F. Ding, J. Wu, Q. Zhang, H. Yang, *Phys. Scr.* **2022**, *97*, 045502.
- [10] W. Cai, U. K. Chettiar, A. V. Kildishev, V. M. Shalaev, *Nat. Photonics* **2007**, *1*, 224.
- [11] S. Ramya, I. S. Rao, *Int. J. Appl. Eng. Res.* **2015**, *10*, 22712.
- [12] A. N. Ibraheem, W. Withawat, J. Infrared, *Millimeter, Terahertz Waves* **2017**, *38*, 1067.

- [13] A. Arash, G. Burak, A. Rajeev, K. M. Yogendra, *Mater. Today* **2020**, *32*, 108.
- [14] N. I. Landy, S. Sajuyigbe, J. J. Mock, D. R. Smith, W. J. Padilla, *Phys. Rev. Lett.* **2008**, *100*, 207402.
- [15] N. R. Han, Z. C. Chen, C. S. Lim, B. Ng, M. H. Hong, *Opt. Express* **2011**, *19*, 6990.
- [16] M. J. Dicken, K. Aydin, I. M. Pryce, L. A. Sweatlock, E. M. Boyd, S. Walavalkar, J. Ma, H. A. Atwater, *Opt. Express* **2009**, *17*, 18330.
- [17] R. Maas, J. Parsons, N. Engheta, A. Polman, *Nat. Photonics* **2013**, *7*, 907.
- [18] Y. M. Qing, H. F. Ma, Y. Z. Ren, S. Yu, T. J. Cui, *Opt. Express* **2019**, *27*, 5253.
- [19] M. Papaioannou, E. Plum, E. T. F. Rogers, N. I. Zheludev, *Light: Sci. Appl.* **2018**, *7*, 17157.
- [20] V. S. Asadchy, I. A. Faniayeu, Y. Ra'di, S. A. Khakhomov, I. V. Semchenko, S. A. Tretyakov, *Phys. Rev. X* **2015**, *5*, 031005.
- [21] G. Eidelstein, N. Fardian-Melamed, V. Gutkin, D. Basmanov, D. Klinov, D. Rotem, Y. Levi-Kalisman, D. Porath, A. Kotlyar, *Adv. Mater.* **2016**, *28*, 4944.
- [22] S. Yoo, Q. H. Park, *Nanophotonics* **2019**, *8*, 249.
- [23] Y. Z. Cheng, Y. L. Yang, Y. J. Zhou, Z. Zhang, X. S. Mao, R. Z. Gong, *J. Mod. Opt.* **2016**, *63*, 1675.
- [24] B. Tang, Z. Li, E. Palacios, Z. Liu, S. Butun, K. Aydin, *IEEE Photonics Technol. Lett.* **2017**, *29*, 295.
- [25] S. Shang, S. Z. Yang, J. Liu, M. Shan, H. L. Cao, *J. Appl. Phys.* **2016**, *120*, 045106.
- [26] H. Tao, C. M. Bingham, D. Pilon, K. Fan, A. C. Strikwerda, D. Shrekenhamer, W. J. Padilla, X. Zhang, R. D. Averitt, *J. Phys. D: Appl. Phys.* **2010**, *43*, 225102.
- [27] J. Zhu, Z. Ma, W. Sun, F. Ding, Q. He, L. Zhou, Y. Ma, *Appl. Phys. Lett.* **2014**, *105*, 021102.
- [28] W. Zhu, X. Zhao, *J. Opt. Soc. Am. B* **2009**, *26*, 2382.
- [29] M. Luo, S. Shen, L. Zhou, S. Wu, Y. Zhou, L. Chen, *Opt. Express* **2017**, *25*, 16715.
- [30] L. Wang, X. Huang, M. Li, J. Dong, *Opt. Express* **2019**, *27*, 25983.
- [31] H. B. Zhang, L. W. Deng, P. H. Zhou, L. Zhang, D. M. Cheng, H. Y. Chen, D. F. Liang, L. J. Deng, *J. Appl. Phys.* **2012**, *112*, 014106.
- [32] Q. Gao, Y. Yin, D. B. Yan, N. C. Yuan, *Electron. Lett.* **2005**, *41*, 936.
- [33] L. Wang, S. Liu, H. Zhang, X. Kong, L. Liu, *J. Electromagn. Waves Appl.* **2017**, *31*, 1216.
- [34] Z. Wang, H. Jia, K. Yao, W. Cai, H. Chen, Y. Liu, *ACS Photonics* **2016**, *3*, 2096.
- [35] H. Tao, A. C. Strikwerda, K. Fan, C. M. Bingham, W. J. Padilla, X. Zhang, R. D. Averitt, *J. Phys. D: Appl. Phys.* **2008**, *41*, 232004.
- [36] J. K. Gansel, M. Thiel, M. S. Rill, M. Decker, K. Bade, V. Saile, M. Wegener, *Science* **2009**, *325*, 1513.
- [37] A. Y. Zhu, W. T. Chen, A. Zaidi, Y. W. Huang, M. Khorasaninejad, V. Sanjeev, C. W. Qiu, F. Capasso, *Light: Sci. Appl.* **2017**, *7*, 17158.
- [38] B. Semnani, J. Flannery, R. A. Maruf, M. Bajcsy, *Light: Sci. Appl.* **2020**, *9*, 23.
- [39] M. Zhijie, L. Yi, L. Yang, G. Yandong, H. Minghui, *Opt. Express* **2018**, *26*, 6067.
- [40] J. Gu, R. Singh, X. Liu, X. Zhang, Y. Ma, S. Zhang, S. A. Maier, Z. Tian, A. K. Azad, H. T. Chen, A. J. Taylor, J. Han, W. Zhang, *Nat. Commun.* **2012**, *3*, 1151.
- [41] C. Menzel, C. Rockstuhl, F. Lederer, *Phys. Rev. A* **2010**, *82*, 053811.
- [42] T. Cao, L. Zhang, R. E. Simpson, C. Wei, M. J. Cryan, *Opt. Express* **2013**, *21*, 27841.
- [43] D. R. Smith, D. C. Vier, T. Koschny, C. M. Soukoulis, *Phys. Rev. E* **2005**, *71*, 036617.